Available online at www.sciencedirect.com
ScienceDirect
Journal of Solid State Chemistry 180 (2007) 2670–2681
JOURNAL OF SOLID STATE CHEMISTRY
www.elsevier.com/locate/jssc

Analysis of the electronic structure of $Hf(Si_{0.5}As_{0.5})As$ by X-ray photoelectron and photoemission spectroscopy

Andrew P. Grosvenor[a,*], Ronald G. Cavell[a], Arthur Mar[a], Robert I.R. Blyth[b]

[a]Department of Chemistry, University of Alberta, Edmonton, Alberta, Canada T6G 2G2
[b]Canadian Light Source, 101 Perimeter Road, University of Saskatchewan, Saskatoon, Saskatchewan, Canada S7N OX4

Received 26 April 2007; received in revised form 17 July 2007; accepted 21 July 2007
Available online 6 August 2007

Abstract

The ternary hafnium silicon arsenide, $Hf(Si_xAs_{1-x})As$, has been synthesized with a phase width of $0.5 \leqslant x \leqslant 0.7$. Single-crystal X-ray diffraction studies on $Hf(Si_{0.5}As_{0.5})As$ showed that it adopts the ZrSiS-type structure (Pearson symbol $tP6$, space group $P4/nmm$, $Z = 2$, $a = 3.6410(5)$ Å, $c = 8.155(1)$ Å). Physical property measurements indicated that it is metallic and Pauli paramagnetic. The electronic structure of $Hf(Si_{0.5}As_{0.5})As$ was investigated by examining plate-shaped crystals with laboratory-based X-ray photoelectron spectroscopy (XPS) and synchrotron radiation photoemission spectroscopy (PES). The Si $2p$ and As $3d$ XPS binding energies were consistent with assignments of anionic Si^{1-} and As^{1-}. However, the Hf charge could not be determined by analysis of the Hf $4f$ binding energy because of electron delocalization in the $5d$ band. To examine these charge assignments further, the valence band spectrum obtained by XPS and PES was interpreted with the aid of TB-LMTO band structure calculations. By collecting the PES spectra at different excitation energies to vary the photoionization cross-sections, the contributions from different elements to the valence band spectrum could be isolated. Fitting the XPS valence band spectrum to these elemental components resulted in charges that confirm that the formulation of the product is $Hf^{2+}[(Si_{0.5}As_{0.5})As]^{2-}$.
© 2007 Elsevier Inc. All rights reserved.

Keywords: Arsenide; Crystal structure; X-ray photoelectron spectroscopy; Photoemission spectroscopy; Electronic structure

1. Introduction

Many metalloid-rich compounds of the form MAB crystallize in the tetragonal structure type known most commonly as the PbFCl- or ZrSiS-type, an ordered ternary variant of the Cu_2Sb-type adopted by metal-rich compounds [1,2]. They can be distinguished by the quantity Δ, the electron deficiency experienced by A and B (after full electron transfer from M) with respect to each attaining an octet [3]. In general, the PbFCl-type designates normal valence compounds where M provides sufficient electrons so that A and B each have an octet ($\Delta = 0$) and form isolated anions, as in $Pb^{2+}F^{1-}Cl^{1-}$. In contrast, the anions in ZrSiS-type compounds must participate in homoatomic bonding to fulfill their octets, as in $Zr^{4+}Si^{2-}S^{2-}$ ($\Delta = 2$) where polyanionic Si–Si bonding is present [4]. Reflecting the more covalent character in bonding, the ZrSiS-type structure is a robust one possessed by many compounds MAB where M is an early transition metal or f-block element (e.g. Zr, Hf, La, Ce) and A and B are heavier p-block elements (e.g. Si, Ge, As, Sb, S, Se, Te) [1]. The A and B sites are subject to substitutional disorder ($Zr(Si_{1-x}As_x)(As_yTe_{1-y})$ [1], $Zr(Si_{0.7}Sb_{0.3})Sb$ [4]) or partial occupancy ($ZrAs_{0.9}(As_{0.5}Se_{0.5})$ [5]).

Electrical and magnetic measurements have revealed diverse properties, including metallic ($ZrAs_{1.4}Se_{0.5}$ [5]), semimetallic (ThPS [6]), semiconducting ($SmTe_{1.8}$ [7]), ferromagnetic (MnAlGe [8]), antiferromagnetic ($USn_{0.5}Sb_{1.5}$ [9]), and paramagnetic (CeSbTe [10]) behaviour. Although spectroscopic studies can also yield valuable information about electronic structure, to our knowledge they have not been made for ZrSiS-type compounds and have been sparse for the related metal-rich Cu_2Sb-type binary compounds. Cu_2Sb itself was initially proposed to be antiferromagnetic [11], but NMR spectroscopy indicated that it is diamagnetic [12], a

*Corresponding author. Fax: +1 780 492 8231.
E-mail address: andrew.grosvenor@ualberta.ca (A.P. Grosvenor).

0022-4596/$ - see front matter © 2007 Elsevier Inc. All rights reserved.
doi:10.1016/j.jssc.2007.07.015

result later confirmed by further magnetic measurements [13]. M_2As (M = Cr, Mn, Fe), Mn_2Sb, and MnAlGe have been examined by photoelectron spectroscopy performed using a laboratory X-ray (XPS), ultraviolet (UPS), or synchrotron radiation source (PES) [8,14,15]. In Mn_2Sb, the valence states of the Mn and Sb sites could be probed separately by adjusting the X-ray energy, thus altering their photoemission cross-sections [14]. Further, the two structurally and magnetically inequivalent Mn sites could be distinguished by the higher binding energy of those atoms that have $3d$ states positioned at the Fermi edge and participate in metal–metal bonding [14].

We have been interested in applying photoelectron spectroscopy to assess the electronic character of atoms in solid state compounds where true charges cannot be as extreme as implied by simple electron-counting formalisms of the type seen above. Nevertheless, through proper interpretation, it is possible to extract information from valence band spectra that can be related to these charges, as we have successfully demonstrated elsewhere for several phosphides and antimonides [16–18]. Here we describe the synthesis, crystal structure, and physical properties of a new ZrSiS-type compound, $HfSi_{0.5}As_{1.5}$, an end-member of the solid solution $Hf(Si_xAs_{1-x})As$ ($0.5 \leqslant x \leqslant 0.7$), and examine its electronic structure through XPS and PES. By analyzing the measured valence band spectra with the aid of band structure calculations, we have evaluated the charges of the constituent atoms and related them to the bonding in this compound, leading to important implications about the electronic structure of ZrSiS-type compounds in general.

2. Experimental

2.1. Synthesis

Powders of Hf (99.6% (excluding 2–4% Zr); Alfa-Aesar), Si (99.99%; Alfa Inorganics), and As (99.9998%; Alfa Inorganics) in the molar ratio 1:0.5:1.5 were sealed in evacuated fused-silica tubes. The samples were heated to 873 K over 12 h, held at this temperature for 3 d, heated to 1173 K over 24 h, and annealed at this temperature for 1–4 weeks. After annealing, the samples were quenched in water. Addition of I_2 (Anachemia) to the reaction as a chemical vapour transport agent (CVT) yielded needle- or plate-shaped crystals depending on the annealing time at 1173 K. SEM–EDX analysis on a Hitachi S-2700 SEM (20 kV beam voltage) revealed that the composition of these crystals was $HfSi_{0.5(1)}As_{1.5(1)}$. Powder X-ray diffraction patterns obtained on an Inel diffractometer equipped with a CPS 120 detector indicated >95% purity of the desired phase, with the remaining <5% mostly containing HfO_2. Use of initial reaction temperatures higher than 873 K led to reaction of Hf with the tube to form larger quantities of HfO_2. When only Hf and As (in either 1:1 or 3:2 ratios) were reacted in a fused-silica tube at 1173 K in the presence of I_2, $Hf(Si_{0.5}As_{0.5})As$ as well as large quantities of HfO_2 and occasionally minor amounts of $HfAs_2$ were produced due to reaction with the tube.

2.2. Structure determination

Single-crystal X-ray diffraction data were collected on a Bruker Platform/SMART 1000 CCD diffractometer at 295 K using ω scans. Structure solution and refinement were carried out with use of the SHELXTL (version 6.12) software package [19]. Face-indexed numerical absorption corrections were applied. The centrosymmetric space group $P4/nmm$ was chosen and initial atomic positions were found by direct methods. Occupying the $2a$ site exclusively with As atoms led to large displacement parameters. If Si and As were assumed to be disordered within this site, the refined occupancies converged to 0.52(1) Si and 0.48(1) As and the displacement parameters became more reasonable. The absence of supercell reflections suggests that Si and As are randomly distributed in this site. The other sites were well behaved.

Atomic positions were standardized with the program STRUCTURE TIDY [20]. Crystal data and further details of the data collection are given in Table 1, final values of the positional and displacement parameters are given in Table 2, and interatomic distances are listed in Table 3. Further data, in CIF format, have been sent to Fachinformationszentrum Karlsruhe, Abt. PROKA, 76344 Eggenstein-Leopoldshafen, Germany, as supplementary material

Table 1
Crystallographic data for $HfSi_{0.5}As_{1.5}$

Formula	$Hf(Si_{0.52(1)}As_{0.48(1)})As$
Formula mass (amu)	304.92
Space group	$P4/nmm$ (No. 129)
a (Å)	3.6410(5)
c (Å)	8.155(1)
V (Å^3)	108.10(3)
Z	2
ρ_{calcd} (g cm^{-3})	9.367
Crystal dimensions (mm)	0.51 × 0.27 × 0.03
Radiation	Graphite monochromated Mo $K\alpha$, $\lambda = 0.71073$ Å
μ(Mo $K\alpha$) (mm^{-1})	70.83
Transmission factors	0.006–0.121
2θ limits	$5.00° \leqslant 2\theta(\text{Mo } K\alpha) \leqslant 65.82°$
Data collected	$-5 \leqslant h \leqslant 5$, $-5 \leqslant k \leqslant 5$, $-12 \leqslant l \leqslant 12$
No. of data collected	1449
No. of unique data, including $F_o^2 < 0$	153
No. of unique data, with $F_o^2 > 2\sigma(F_o^2)$	153
No. of variables	11
$R(F)$ for $F_o^2 > 2\sigma(F_o^2)$[a]	0.028
$R_w(F_o^2)$[b]	0.068
Goodness of fit	1.306
$(\Delta\rho)_{max}$, $(\Delta\rho)_{min}$ (e Å^{-3})	3.60, −2.85

[a] $R(F) = \Sigma||F_o| - |F_c||/\Sigma|F_o|$.
[b] $R_w(F_o^2) = [\sum[w(F_o^2 - F_c^2)]/\sum wF_o^4]^{1/2}$, $w^{-1} = [\sigma^2(F_o^2) + (0.0419p)^2 + 0.2623p]$ where $p = [\max(F_o^2, 0) + 2F_c^2]/3$.

Table 2
Atomic coordinates and equivalent isotropic displacement parameters for $Hf(Si_{0.5}As_{0.5})As$

Atom	Wyckoff position	Occupancy	x	y	z	U_{eq} (Å^2)[a]
Hf	2c	1	$\frac{1}{4}$	$\frac{1}{4}$	0.25606(6)	0.0092(3)
Si/As1	2a	0.52(1)/0.48(1)	$\frac{3}{4}$	$\frac{1}{4}$	0	0.0114(6)
As2	2c	1	$\frac{1}{4}$	$\frac{1}{4}$	0.6148(2)	0.0086(4)

[a] U_{eq} is defined as one-third of the trace of the orthogonalized U_{ij} tensor.

Table 3
Selected interatomic distances (Å) in $Hf(Si_{0.5}As_{0.5})As$[a]

Hf–As2 (×4)	2.7545(6)
Hf–As2	2.852(1)
Hf–X (×4)	2.8260(5)
X–X (×4)	2.5746(4)

[a] X represents the disordered site containing 0.5 Si and 0.5 As1.

No. CSD-418329 and can be obtained by contacting FIZ (quoting the article details and the corresponding CSD numbers).

2.3. Property measurements

The electrical resistivity along the length of a flat needle-shaped crystal (corresponding to the symmetry-equivalent [1 0 0] or [0 1 0] directions, or the in-plane resistivity, ρ_{ab}) having dimensions $1.9 \times 0.2 \times 0.1\,mm^3$ was measured from 2 to 300 K by standard four-probe techniques on a Quantum Design PPMS system equipped with an ac transport controller (Model 7100). The current was 100 μA and the frequency was 16 Hz. Measurement of the out-of-plane resistivity ρ_c was precluded by the habit and dimensions of the available crystals. The magnetic susceptibility was measured on a ground sample of the crystals (~100 mg) from 2 to 300 K on a Quantum Design 9T-PPMS dc magnetometer/ac susceptometer under a 10 kOe field. The susceptibility was corrected for contributions from the holder and the core diamagnetism of the sample.

2.4. X-ray photoelectron spectroscopy (XPS)

XPS measurements were made on a Kratos AXIS 165 spectrometer fitted with a monochromatic Al Kα X-ray (1486.7 eV) source. The resolution of this instrument has been determined to be 0.4 eV [16]. The typical precision of binding energies (BE) in this instrument is better than ±0.1 eV and the area analyzed was $\sim 700 \times 400\,\mu m^2$. The angle between the X-ray source and hemispherical analyser was 54.7°.

Plate-shaped crystals (each with surface area $>1 \times 1\,mm^2$) were affixed onto a Cu sample holder by C tape. The samples were connected with silver paint (DuPont Electronics) directly to the Cu holder, ensuring electrical contact with ground to minimize charging effects. After being loaded into the spectrometer, the samples were cleaned by Ar^+ ion sputtering (4 kV accelerating voltage, 1–10 mA current) to reduce the concentration of surface oxides and other contaminants (e.g. C, I) present. Different currents were used to evaluate whether preferential sputtering of the light elements or reduction occurred. Neither effect was observed and survey spectra from multiple samples indicated the composition of the surface was $HfSi_{0.6(1)}As_{1.3(2)}$, which agrees with the bulk composition when the accuracy of the measurement is considered. The samples were not annealed after sputter-cleaning because the constituent elements (particularly Hf, but also Si) were found to be quite reactive in the vacuum chamber of the spectrometer at room temperature, even though the base pressure was $\sim 10^{-7}$ Pa, producing small amounts of surface oxide over time. This phenomenon has also been observed during XPS studies of Hf metal [21]. Annealing would only enhance this contamination and so was not performed. High-resolution spectra of the As 3d, Si 2p, and Hf 4f core lines and of the valence band were collected with a pass energy of 20 eV, a step size of 0.05 eV, a sweep time of 180 s, and an energy envelope of 10–20 eV. All spectra were analysed with the CasaXPS software program [22]. During data analysis, the samples were calibrated using the C 1s line arising from adventitious C with a fixed value of 284.8 eV. Because As Auger signals overlap the C 1s line in this system, the calibration was checked by setting the maximum of the first derivative of the valence band on the low BE side of the spectrum to 0 eV, which represents the Fermi edge. This is an accepted calibration method for metallic compounds such as the one under study [23]. A Shirley-type function was applied to remove the background arising from energy loss and spectra were fitted using a combined Gaussian (70%) and Lorentzian (30%) line profile. For comparison purposes, the Hf 4f spectrum from Hf metal (99.5% (excluding 3% Zr); Alfa-Aesar) was also collected using the same sample preparation and XPS settings discussed above.

2.5. Photoemission spectroscopy (PES)

Valence band photoemission spectra at different X-ray excitation energies (from 500 to 255 eV) were collected at the Canadian Light Source (CLS) in Saskatoon, Saskatchewan, using the spherical grating monochromator (SGM) undulator beamline, 11-ID.1 [24], and a Scienta 100

hemispherical analyser equipped with a channel plate detection system. Changing the excitation energies modulates the photoionization cross-section and separates the valence contributions arising from Hf, As, and Si. The monochromatized photon flux of this beamline is $\sim 10^{12}$ photons/s at 250 eV and 5×10^{12} photons/s at 500 eV. An aggregate of needle-shaped crystals was mounted on the sample holder with TorrSeal epoxy. Because the sample is insulated by the epoxy, it was connected with C tape to the grounded stage to reduce charging effects. After curing, the sample was loaded into the introduction chamber attached to the analytical chamber of the spectrometer. Once a suitable pressure was achieved in the introduction chamber ($\sim 10^{-7}$ Pa), the sample was scraped *in situ* in the introduction chamber using glass paper to produce a clean surface appropriate for photoemission experiments and then transferred to the analysis chamber. The cleanliness of the sample was monitored by examining the Hf 4*f* spectrum. The valence band spectra were measured with a pass energy of 100 eV, an energy step size of 0.02 eV, and a dwell time of 33 ms. At 500 eV, the overall resolution, including analyser and beamline contributions, was ~0.16 eV, measured using the Fermi edge of a clean Au sample. The beamline exit setting used, 20 μm, gives a spot size on the sample of ~1 mm × 80 μm. Resonant photoemission was performed by examining the valence band with an excitation energy equal to the Hf N_3 ($4p_{3/2}$) absorption peak (384 eV), which was determined by collecting a total electron yield (TEY) X-ray absorption spectrum, compared to that obtained with an excitation energy just below the absorption edge (360 eV). To directly compare the spectra, all signal intensities were normalized to the incident photon flux. Because the sample is metallic, all valence band spectra were aligned by setting the maximum in the first derivative of the low-binding energy side of the spectra to be equal to 0 eV (Fermi edge).

2.6. Band structure calculations

To help interpret the valence band spectra, tight-binding linear muffin–tin orbital band structure calculations were performed within the atomic spheres approximation (TB-LMTO ASA) [25]. Contributions from the Si 3*s*, 3*p*; As 4*s*, 4*p*; and Hf 5*d* orbitals to the density of states were extracted. Because mixed occupancy is problematic to treat, three ordered models were considered in which the disordered site is occupied by: (i) As atoms only ("$HfAs_2$"), (ii) Si atoms only ("HfSiAs"), or (iii) alternating Si and As atoms with only heteroatomic Si–As bonding present ("$Hf(Si_{0.5}As_{0.5})As$"). In the last model, the space group was chosen to be $P\bar{4}m2$ (No. 115) and the atomic positions were: Hf, 2*g* ($\frac{1}{2}$, 0, −0.2651); Si, 1*b* ($\frac{1}{2}$, $\frac{1}{2}$, 0); As1, 1*a* (0, 0, 0); As2, 2*g* ($\frac{1}{2}$, 0, 0.3851). The calculations were performed with 245 *k* points in the irreducible portion of the Brillouin zone for the first model and 1152 *k* points for the other two models.

3. Results and discussion

3.1. Synthesis and crystal structure

$Hf(Si_{0.5}As_{0.5})As$ is a new ZrSiS-type representative, augmenting the three other examples, $ZrSi_{0.7}Sb_{1.3}$, ZrGeSb, and HfGeSb [4,26], known in the ternary systems (Zr, Hf)–(Si, Ge)–(As, Sb). As in the synthesis of other Si-containing compounds of this structure type [1,4], $Hf(Si_{0.5}As_{0.5})As$ can also be formed through a deleterious reaction of Hf and As with the fused-silica tube at high temperature. The nonstoichiometry suggests the possibility of a phase width, which was investigated by carrying out a series of reactions with compositions $Hf(Si_xAs_{1-x})As$ ($0.1 \leqslant x \leqslant 1$). Powder XRD analysis established a small homogeneity range of $0.5 \leqslant x \leqslant 0.7$ where single-phase $Hf(Si_xAs_{1-x})As$ was formed. Below $x = 0.5$, $HfAs_2$ and $Hf(Si_{0.5}As_{0.5})As$ were formed, whereas above $x = 0.7$, $Hf(Si_{0.7}As_{0.3})As$ was found with Si and HfAs. The cell parameters, calculated using the program UNITCELL [27], range from $a = 3.6279(6)$ Å and $c = 8.135(2)$ Å for $Hf(Si_{0.5}As_{0.5})As$ to $a = 3.6115(5)$ Å and $c = 8.160(2)$ Å for $Hf(Si_{0.7}As_{0.3})As$. The ZrSiS-type structure adopted by MAB compounds such as $Hf(Si_{0.5}As_{0.5})As$, shown in Fig. 1, can be described in terms of a stacking of square nets, those containing the A (Si/As1) atoms being twice as dense as those containing the M (Hf) or B (As2) atoms. The distances within the denser square net (2.5746(4) Å) are indicative of weak bonding, whereas those within the other nets (3.6410(5) Å, equal to the *a* parameter) are too far to

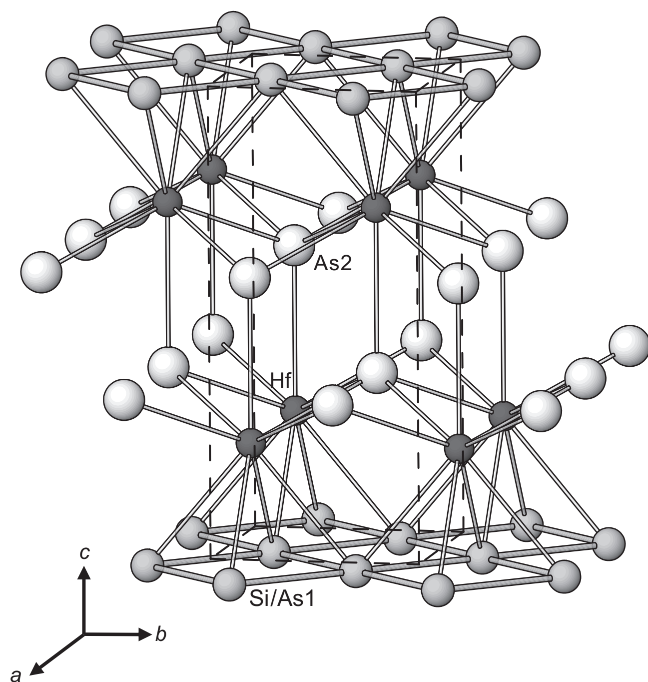

Fig. 1. Structure of $Hf(Si_{0.5}As_{0.5})As$ viewed down the *a* direction. Like other MAB compounds with the ZrSiS-type structure, it consists of a stacking of nets of M (Hf), A (Si/As1), and B (As2) atoms.

be significant. The disorder of Si and As atoms within the A net implies that Si–Si, Si–As, and As–As bonding are operative. The Hf atoms are nine-coordinate, at the centres of monocapped square antiprisms connected in a head-to-head and tail-to-tail configuration. The distance to the capping atom (2.852(1) Å) is only slightly longer than to the other atoms (2.7545(6)–2.8260(5) Å), implying strong bonding along all directions in the structure.

Size effects account for some of the structural features in $Hf(Si_{0.5}As_{0.5})As$. Si and As have sufficiently similar sizes (metallic radii $R_1 = 1.17$ Å for Si, 1.21 Å for As [28]) that they readily disorder within the denser A net, but the less dense B net contains exclusively the slightly larger As atoms. An analogous type of disorder has been observed previously in $Zr(Si_{1-x}As_x)(As_yTe_{1-y})$ [1]. As seen above in the trends in cell parameters, as the larger As atoms are substituted for Si in the denser square net on going from $Hf(Si_{0.7}As_{0.3})As$ to $Hf(Si_{0.5}As_{0.5})As$, the expansion of a is accompanied by a contraction in c, which is related to the relief of steric crowding as the Hf-centred square antiprisms become flattened to allow the capping atoms to approach more closely [1]. The absence or presence of this interaction with the capping ligand has been used to classify ZrSiS-type structures as 2D or 3D, respectively, the transition occurring at a critical c/a ratio of ~2.3 [1]. For $Hf(Si_xAs_{1-x})As$ ($0.5 \leqslant x \leqslant 0.7$), the c/a ratios of 2.24–2.26 are lower than the critical value and consistent with a 3D structure.

Electronic effects also play an important role, through the optimization of homoatomic and heteroatomic bonding interactions within and between the square nets. In ZrSiS-type structures, electronic stabilization is favoured by placement of the less electronegative main-group element in the denser A net [2], consistent with the observed structure of $Hf(Si_{0.5}As_{0.5})As$. In some cases, geometrical distortion of the square net occurs to maximize bonding, as in GdPS or $SmTe_{1.84}$ [2,7], but this does not happen in $Hf(Si_{0.5}As_{0.5})As$. The Si/As disorder in the $2a$ site spans only a narrow range (0.7:0.3–0.5:0.5) and the parent binary phases adopt structure types ($HfSi_2$ ($ZrSi_2$-type); $HfAs_2$ ($PbCl_2$-type) [29]) different from the ternary phase, satisfying two of the criteria invoked by the concept of differential fractional site occupancy (DFSO) stabilization [30]. Although cationic DFSO-stabilized materials are now well known [30,31], anionic DFSO-stabilized materials such as $Hf(Si_{0.5}As_{0.5})As$ are still relatively rare [31,32]. The different structure type adopted by $Hf(Si_{0.5}As_{0.5})As$ can be attributed to a competition between the anion–anion (Si–Si, As–As, Si–As) bond energies and the configurational (non-kinetic) entropy of the disordered site [30]. The distances within the denser A net in $Hf(Si_{0.5}As_{0.5})As$ are somewhat longer than typical Si–Si (2.3 Å) or As–As (2.4 Å) covalent bonds [28], lowering the contribution of the bond enthalpy. However, the random distribution of Si and As atoms within this net raises the configurational entropy, providing a stabilization of the Gibbs free energy of the system.

3.2. Electrical and magnetic properties

Most ZrSiS-type compounds are expected to be metallic, as predicted by band structure calculations on this (*vide infra*) and related members [2]. The profile of the in-plane electrical resistivity (ρ_{ab}) for a single crystal of $Hf(Si_{0.5}As_{0.5})As$, shown in Fig. 2a, confirms metallic behaviour. The resistivity values are relatively high ($\rho_{300\,K} = 1.9 \times 10^{-4}\,\Omega\,cm$) and the residual resistivity ratio ($RRR = \rho_{300\,K}/\rho_{2\,K} = 2.0$) is small, consistent with the high degree of disorder in this material. The magnetic susceptibility curve, shown in Fig. 2b, indicates essentially temperature-independent Pauli paramagnetism ($\chi = 8 \times 10^{-4}$ emu/mol), with a slight upturn at low temperatures most likely arising from small amounts of paramagnetic impurities.

3.3. Electronic structure

In $Hf(Si_{0.5}As_{0.5})As$, if Hf is assumed to transfer four valence electrons, the Si and As atoms together are still deficient by $\Delta = 2.5$ electrons relative to filled octets. The

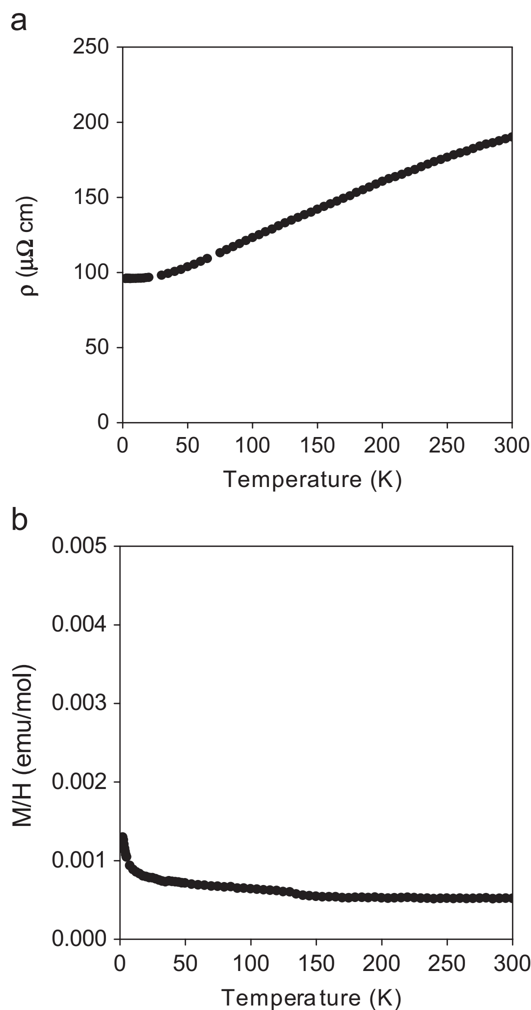

Fig. 2. (a) Electrical resistivity (within the *ab* plane) and (b) magnetic susceptibility of $Hf(Si_{0.5}As_{0.5})As$.

As atoms in the B net are too far apart (3.6410(5) Å) to be bonding and can be assigned to be isolated As^{3-} anions. A charge-balanced ionic formulation would thus be $Hf^{4+}(Si_{0.5}As_{0.5})^{1-}As^{3-}$, implying that anion–anion bonding must develop within the A net among the disordered Si and As atoms to complete their octets. Although the distances within the A net (2.5746(4) Å) are smaller than those within the B net, they are certainly still too long to be considered $2c$–$2e^-$ Si–Si, Si–As, or As–As bonds (~2.4 Å [28]). These distances are instead consistent with multi-centre bonding of fractional bond character. Within such hypervalent bonded square nets, the ideal electron count is six, corresponding to the presence of "one-electron bonds" [2]. This electron count is consistent with the charge assignment of As^{1-} but not quite with Si^{1-}; however, a slight deviation is energetically permissible given that only non-bonding or weakly antibonding levels are affected. Although simple electron-counting schemes such as this are helpful in developing a first approximation to the electronic structure and can be remarkably successful in rationalizing bonding in complex solid-state structures, they overemphasize the degree of charge transfer that takes place. True charges are not expected to be as extreme as implied by these ionic formulations, and it is our goal to evaluate charges, by experimental means and assess the validity of this approach.

3.3.1. As 3d and Si 2p XPS spectra

The As $3d$ core-line spectrum of $Hf(Si_{0.5}As_{0.5})As$ is shown in Fig. 3a. There is only one signal, split into a doublet representing the $3d_{5/2}$ and $3d_{3/2}$ spin–orbit coupled final states, which were fitted with two peaks each having a FWHM of ~0.9 eV in an intensity ratio equal to the theoretical value of 3:2. On the high BE side of the spectrum, the asymmetric lineshape may be attributed to contributions from As suboxides formed during the experiment (as has also been observed in surface studies of GaAs [33]), or it may be related to the metallic nature of $Hf(Si_{0.5}As_{0.5})As$, as discussed below in the context of the Hf spectrum.

The BE of the As $3d_{5/2}$ peak is 40.8 eV, which is considerably lower than that in elemental As (41.7(2) eV [34]) (dashed line in Fig. 3a), indicating that As is anionic in $Hf(Si_{0.5}As_{0.5})As$. In comparison to the BE of other As-containing compounds having known charges (e.g. As, As_2O_3, As_2O_5) [34] and assuming a linear relationship, this value indicates an estimated As charge of approximately 1–. The presence of only one signal suggests that both As1 and As2 atoms adopt the same charge, contrary to the prediction made by the electron-counting scheme described above. The lower than expected charge implies significant covalent character in the Hf–As bonds and incomplete charge transfer from Hf to As. Caution must be exercised in interpreting charges derived from binding energies. Although binding energies are principally influenced by the charge on the atom of interest, they also depend on other factors such as the identity of the ligand, variations in the coordination environment, and final state relaxation effects [23]. For example, the As $3d_{5/2}$ BE is 45.3 eV in $AsBr_3$ and 47.1 eV in AsF_3 [34], a substantial difference even though the nominal charge of As is 3+ in both compounds. Other analyses must therefore be performed, as described below, to substantiate the charge assignments derived from core-line binding energies.

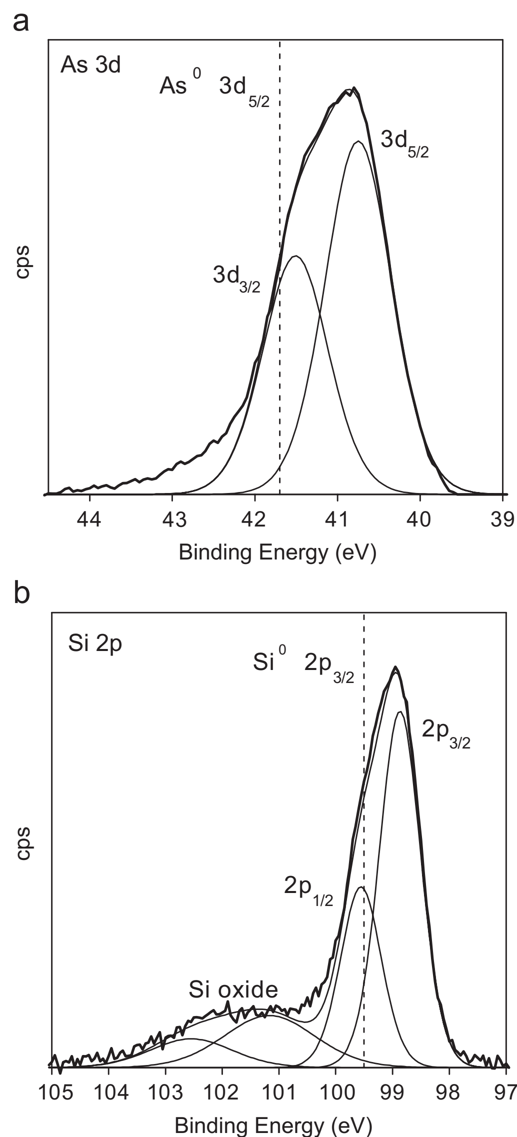

Fig. 3. (a) As $3d$ and (b) Si $2p$ core-line spectra of $Hf(Si_{0.5}As_{0.5})As$, fitted with component peaks representing the spin–orbit coupled final states. The binding energy of elemental As or Si is marked by a vertical dashed line.

The Si $2p$ core-line spectrum (Fig. 3b) also shows one set of spin–orbit split peaks, representing the $2p_{3/2}$ and $2p_{1/2}$ final states, fitted with a FWHM of ~0.8 eV in an intensity ratio of 2:1. The Si $2p_{3/2}$ BE is 98.9 eV, about 0.6 eV lower than that in elemental Si (99.5(3) eV [34]) (dashed line in Fig. 3b) and indicative of anionic Si. As before, binding energies were compared with other Si-containing compounds [34], resulting in an estimated Si charge of approximately 1− in $Hf(Si_{0.5}As_{0.5})As$. The Si $2p_{3/2}$ BE in

$Hf(Si_{0.5}As_{0.5})As$ is similar to that in $TiSi_2$ [35]. As well, the valence band spectrum of $TiSi_2$ reveals occupied Ti 3*d* states [35], implying the Si charge is not as large as 2−, as predicted by simple electron counting.

The smaller negative BE shift relative to the elements observed for the Si $2p_{3/2}$ line ($\Delta BE = 0.6$ eV) than for the As $3d_{5/2}$ line ($\Delta BE = 0.9$ eV) can be related to the difference in electronegativity between Si and As [28]. Because As is more electronegative, it attracts a greater amount of electron density from the neighbouring Hf and Si atoms, lowering the As 3*d* BE. On the other hand, because Si is less electronegative, the Hf–Si bonds are more covalent than the Hf–As bonds which reduces the screening of the Si nuclear charge by the valence electrons.

On the high BE side, the Si 2*p* spectrum (Fig. 3b) also contains a component fitted by split $2p_{1/2}$ and $2p_{3/2}$ spin–orbit peaks, which may be attributed to Si oxides formed during data collection by reaction of the surface with residual oxygen in the vacuum chamber. Although the $2p_{3/2}$ BE of 101.2 eV is much lower than in bulk SiO_2 (103.5(3) eV [34]), it is similar to that in Si suboxides observed during analysis of Si nanocrystals [36,37]. Only one set of broad spin–orbit split peaks was used to represent the Si suboxide component even though it is known that such oxides can have a variety of Si charges [37].

3.3.2. Hf 4f XPS spectra

The Hf 4*f* spectrum of $Hf(Si_{0.5}As_{0.5})As$ (Fig. 4a) is compared with that of Hf metal (Fig. 4b). Both spectra show two asymmetric spin–orbit coupled final states, $4f_{7/2}$ and $4f_{5/2}$, fitted by component peaks with a FWHM of ~0.7–0.8 eV in a fixed intensity ratio of 4:3. The asymmetric lineshapes are characteristic of not only metallic compounds but also small band-gap semiconductors that possess a delocalized electronic structure [16,17]. First described by Doniach and Šunjić, this asymmetry arises when valence electrons, interacting with the core hole, are excited and scattered from filled states below the Fermi edge into empty conduction states [38]. Metallic compounds, such as $Hf(Si_{0.5}As_{0.5})As$, have a continuum of states above the Fermi edge, so that an asymmetric tail comprising many closely spaced states is observed instead of a few distinct satellite peaks [39]. In addition to the asymmetric peaks, other states at higher BE are seen in the spectra and may be attributed, as in the case of the Si 2*p* spectrum above, to small amounts of metal suboxide contamination. Sputter-cleaned Hf metal shows the same behaviour [21].

The Hf $4f_{7/2}$ BE is 14.8 eV in $Hf(Si_{0.5}As_{0.5})As$, higher than in Hf metal (14.2 eV) and consistent with cationic Hf. The magnitude of this shift is smaller than expected for a Hf charge of 4+ (obtained from simple electron counting). For comparison, the measured Hf $4f_{7/2}$ BE for HfO_2 (Alfa-Aesar) is 16.7 eV. The delocalized electronic structure of $Hf(Si_{0.5}As_{0.5})As$, which is metallic, gives rise to very effective screening of the Hf nuclear charge, complicating the assignment of the Hf atomic charge solely on the basis of a BE analysis.

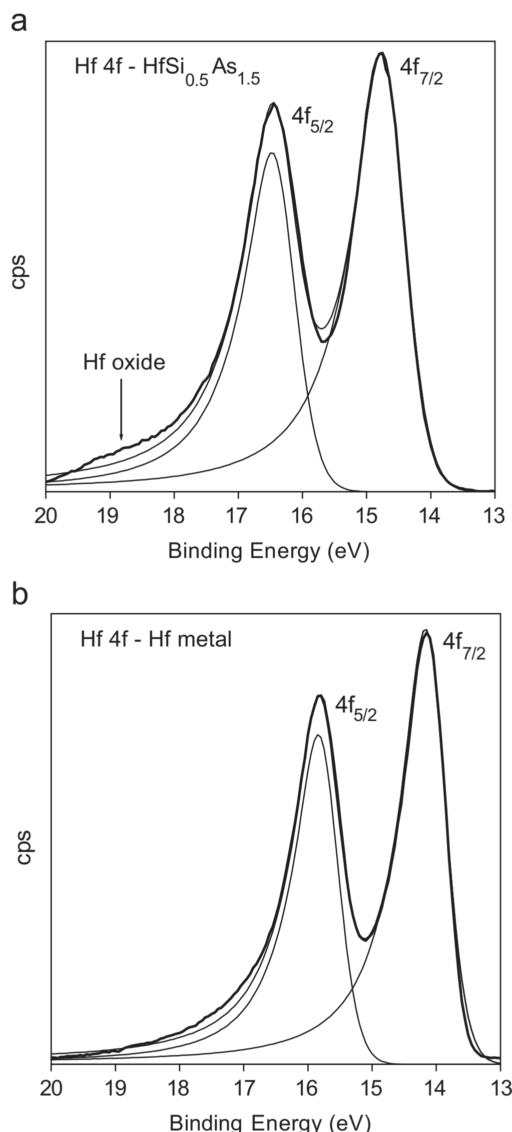

Fig. 4. Hf 4*f* core-line spectra of (a) $Hf(Si_{0.5}As_{0.5})As$ and (b) Hf metal, fitted with asymmetric component peaks representing the $4f_{7/2}$ and $4f_{5/2}$ final states.

3.3.3. Valence band XPS spectra and LMTO band structure calculations

When the core-line binding energy shifts do not give definitive information about valence states and when covalent bonding is significant, analysis of the valence band spectra can provide useful insight about the electronic structure, as we have shown elsewhere in previous studies of intermetallic compounds [16–18]. The valence band spectrum of $Hf(Si_{0.5}As_{0.5})As$ is shown in Fig. 5, with its components labelled from 1 to 4. To interpret these components, the spectrum can be compared with band structures calculated for three ordered models differing in the occupancy of the disordered site and thereby the type of bonding interactions present in the denser square net: (i) "$HfAs_2$" (As–As bonding only), (ii) "HfSiAs" (Si–Si bonding only), and (iii) "$Hf(Si_{0.5}As_{0.5})As$" (Si–As bonding only) (Fig. 6). All three models reproduce the general

features of the valence band spectrum, if variations in the photoionization cross-sections of different elements, which affect intensities [40], are taken into consideration.

The low intensity shoulder (component 1) is located at the Fermi edge (0 eV), consistent with the metallic nature of this compound. The band structures reveal occupied Hf 5*d* states in the valence band, arguing against the presence of Hf^{4+}. The intense broad peak (component 2) represents As 4*p* and Si 3*p* states. The low BE part of this peak originates from As2 4*p* states of the less dense square net, whereas the high BE part originates from Si 3*p* and As1 4*p* states of the denser square net. The difference in energy arises because stronger bonding interactions in the denser square net stabilize the Si/As1 states (thus increasing their BE). If only Si–As bonding is active in this square net, the Si 3*s* states lie higher in energy than the As2 4*s* states (Fig. 6c) but introduction of Si–Si bonding shifts the Si 3*s* states to lower energy so that they overlap the As2 4*s* states (Fig. 6b). Thus, component 3 in Fig. 5 is assigned to have contributions from both Si 3*s* and As2 4*s* states. Finally, component 4 is unambiguously assigned to arise from As1 4*s* states, which occur at the deepest energies in the band structures (Figs. 6a and c).

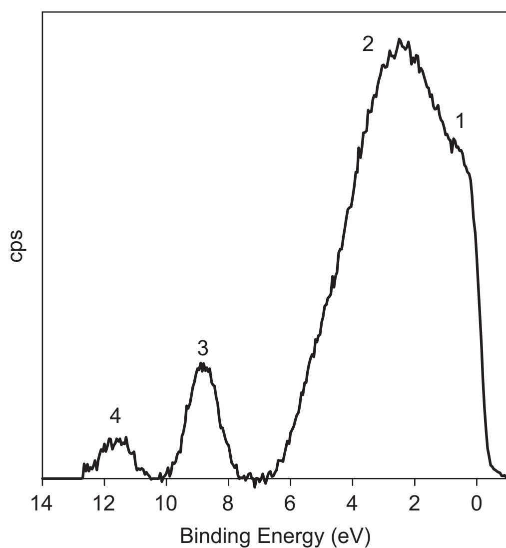

Fig. 5. XPS valence band spectrum of $Hf(Si_{0.5}As_{0.5})As$ collected using Al $K\alpha$ X-rays.

3.3.4. Photoemission spectroscopy (PES)

In Fig. 5, the sharpness of the low BE shoulder (component 1) representing Hf 5*d* states suggests that only a single Hf $5d_{5/2}$ peak instead of a spin–orbit doublet ($5d_{5/2}$ and $5d_{3/2}$) is present in this region. This feature was investigated further with resonant PES conducted on the SGM beamline at the CLS. Resonant photoemission exploits optically allowed ($\Delta l = \pm 1$) transitions from a core level to a partially occupied band. If the occupancy of the Hf 5*d* band is *N*, then at photon energies where a Hf 4*p* core level electron can be excited into an empty 5*d* state, two possible photoemission processes can co-exist. In addition to the "normal" photoemission process, $4p^6 5d^N + h\nu \rightarrow 4p^6 5d^{N-1} + e^-$, the $5d^{N+1}$ excited state that can also be reached with appropriately selected photon

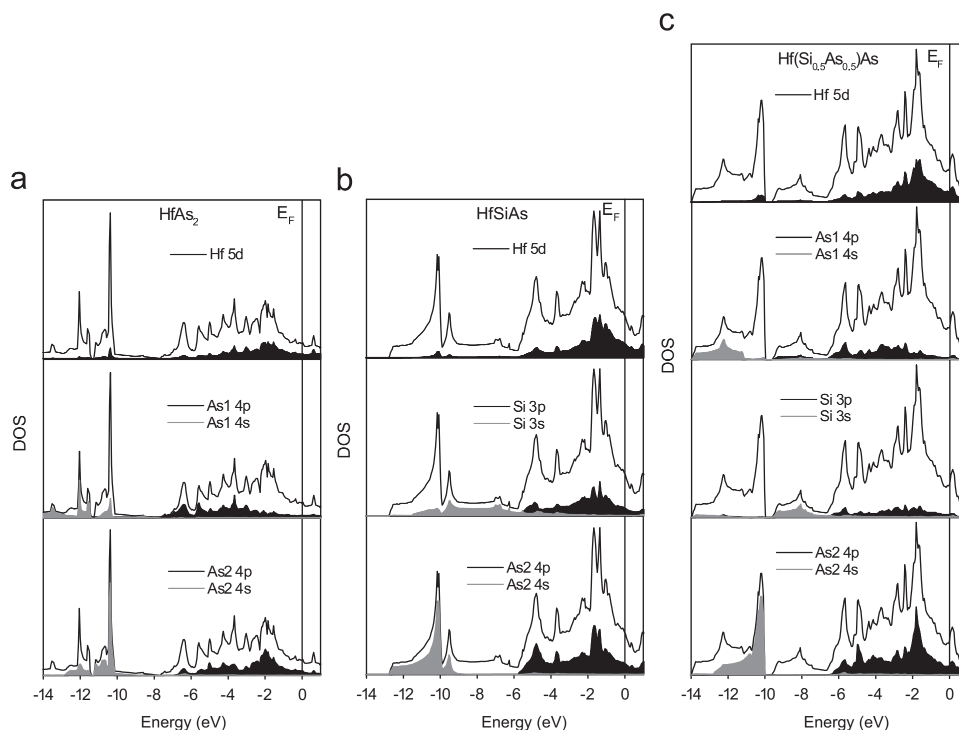

Fig. 6. Band structures of (a) $HfAs_2$, (b) HfSiAs, and (c) $Hf(Si_{0.5}As_{0.5})As$. The projections of different states are shown by the shaded regions and the total density of states by the thin line.

energies can decay via an autoionization process: $4p^65d^N + hv \rightarrow 4p^55d^{N+1} \rightarrow 4p^65d^{N-1} + e^-$. The final state of this process is the same as that in the normal photoemission process, i.e. single ionization, not the double ionization produced by a normal Auger decay, and by conservation of energy the emitted electrons have the same kinetic energy as those of the "normal" photoemission process. The practical result is an increase in the 5*d* photoemission signal at photon energies corresponding to allowed 4*p*–5*d* transitions. The effect is well known, and very large, for 4*d*–4*f* transitions in lanthanide materials [41,42], but is also observed as a smaller, but significant, effect for other allowed transitions, e.g. 3*p*–3*d* in Ti [43] and 4*f*–5*d* in Ir [44].

Fig. 7 shows the resonant photoemission spectra of $Hf(Si_{0.5}As_{0.5})As$ collected using an excitation energy of 384 eV (equal to the Hf N_3 ($4p_{3/2}$) absorption peak as determined by a X-ray absorption measurement) and 360 eV (below the Hf N_3 absorption edge). The region of the valence band spectra shown represents where the Hf 5*d* and As2 4*p* states were proposed to reside, based on comparison of Figs. 5 and 6. As can be seen, the peak found at the Fermi edge (0 eV) is enhanced when the excitation energy is increased from 360 to 384 eV, providing further evidence that it represents an Hf 5*d* state. Between 4 and 1 eV, there is also a small enhancement, implying contributions of the Hf 5*d* band in this region. The enhancement is not as large as would be expected if the excitation energy were equal to that of the 5*p* absorption edge, because the lifetime of the autoionization decay process experienced here is longer than that of a Coster-Kronig decay process [45]. Nevertheless, the increase in the Hf 5*d* intensity is greater than would be expected on the basis of only the difference in Hf 5*d* and As 4*p* photoionization cross-sections at the two energies [40].

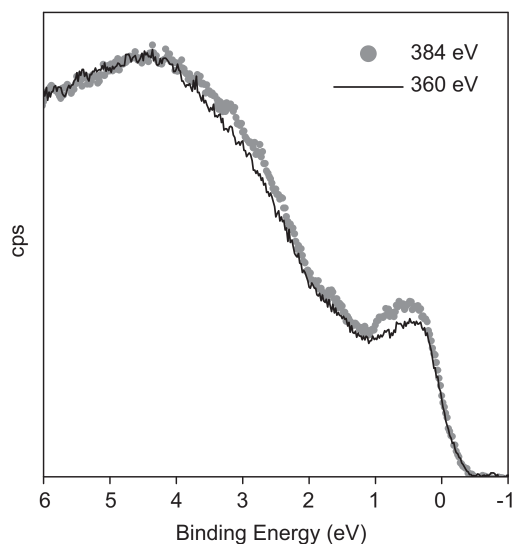

Fig. 7. Resonant PES spectra of $Hf(Si_{0.5}As_{0.5})As$ collected using an excitation energy equal to the Hf N_3 ($4p_{3/2}$) absorption edge (384 eV) and one just below the absorption edge (360 eV). The spectral intensities have been normalized to account for differences in incident photon flux.

The valence contributions in $Hf(Si_{0.5}As_{0.5})As$ were further assessed by varying the excitation energy, which changes the orbital photoemission cross-sections (Fig. 8a) of different elements, allowing them to be identified. Valence band spectra collected at different excitation energies ranging from 500 to ~250 eV are shown normalized to the As2 4*p* intensity (Fig. 8b). Although the surface was scraped in vacuum, a small amount of surface oxide was present, limiting our ability to examine the As1 4*p*/Si 3*p* and As 4*s*/Si 3*s* components. However, the region from 0 to 6 eV was unobscured, permitting identification of the Hf 5*d* and As2 4*p* states. As the excitation energy was changed from 500 to 255 eV, the intensity of the Hf 5*d* peak located at the Fermi edge diminishes significantly compared to the As2 4*p* peak, in accordance with the variation in cross-sections (Fig. 8a). The reduction in intensity indicates that the region from 4 to 0 eV has contributions from Hf 5*d* states, in agreement with the resonant photoemission results. If the feature located at the Fermi edge is identified to be the Hf $5d_{5/2}$ peak, then the higher BE signal can be assigned to be the $5d_{3/2}$ peak (i.e. a

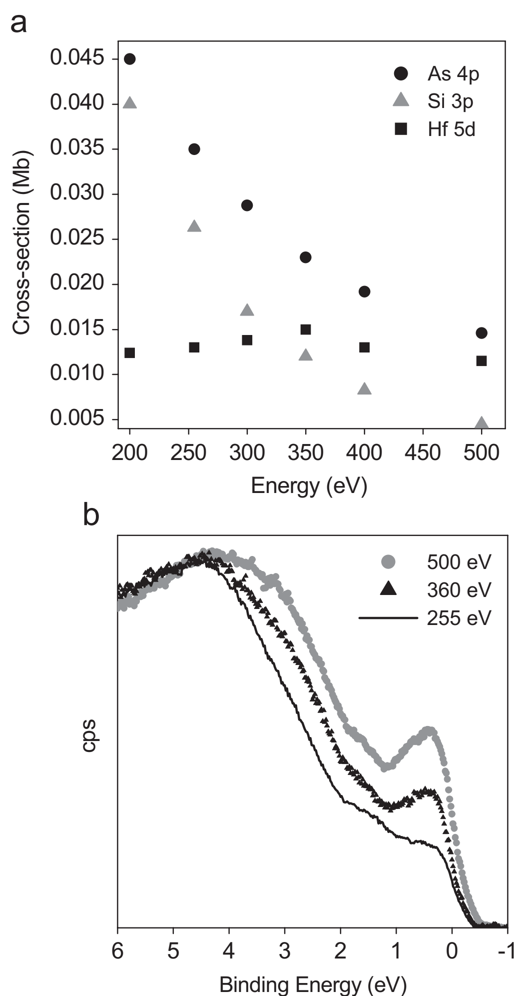

Fig. 8. (a) Variation in the Hf 5*d*, As 4*p*, and Si 3*p* photoionization cross-sections from 250 to 500 eV [40] and (b) PES valence band spectra collected using excitation energies equal to 255, 360, and 500 eV. The spectra have been normalized to the As2 4*p* peak.

Hf 5*d* spin–orbit doublet is observed). These results provide further evidence against a Hf^{4+} species.

3.3.5. Fitting of the valence band spectrum

The core-line binding energies indicate charges of 1− for Si and As, and the valence band spectra (XPS and PES) indicate a charge of 2+ for Hf, as implied by the presence of occupied Hf 5*d* states and by charge balance with the anions. These charge assignments can be tested further by fitting the valence band spectrum. This type of analysis has proven useful in extracting the atomic charges in other intermetallic compounds [16–18]. As shown in Fig. 9, the valence band spectrum was fitted with component peaks (labelled 1–6) representing the different states identified by PES and the band structure calculations. Peaks 1 and 2 represent the Hf $5d_{5/2}$ and $5d_{3/2}$ spin–orbit doublet, fitted with asymmetric lineshapes in accordance with similar profiles observed in the Hf 4*f* spectrum (Fig. 4a) and consistent with what has been observed in the valence band spectra of other transition metals [16]. The peak splitting was determined to be ~1 eV on the basis of the PES spectra (Fig. 8b). Peak 3 represents the As 2*p* component. Peak 4 represents the Si 3*p* and As1 4*p* components. Because the separation between the spin–orbit split states, $np_{3/2}$ and $np_{1/2}$, is small, only a single peak was used to simplify the fitting of the *np* states. Peak 3 is more intense than peak 4 because the cross-section for As 4*p* is larger than for Si 3*p* when an excitation energy equal to that of Al *K*α X-rays is used (Table 4); ultimately, the difference in peak intensity depends on the ratio of As2 to As1 atoms, 2:1. Peak 5 represents both As2 4*s* and Si 3*s* states, and peak 6 represents the As1 4*s* state, on the basis of comparing the valence band spectrum to the band structure calculations (Fig. 6).

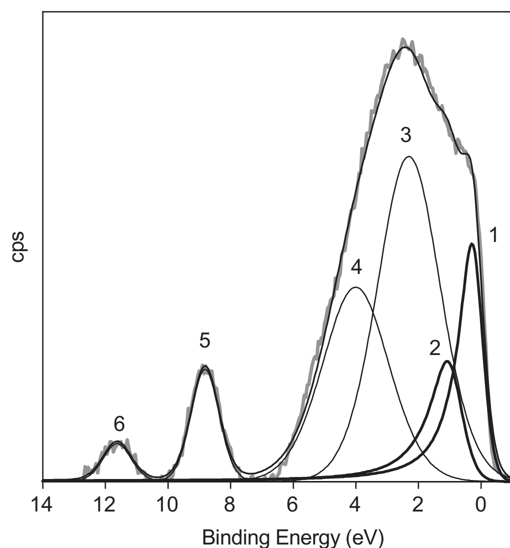

Fig. 9. Fitted XPS valence band spectrum of $Hf(Si_{0.5}As_{0.5})As$ collected using Al *K*α X-rays. The assignments of the peaks labelled from 1 to 6 are discussed in the text and listed in Table 5. The spectrum is represented by a thick grey line and the fitted envelope by a thin black line.

Table 4
Atomic photoelectron cross-sections (σ)[a,b]

Reference	[40]	[47]
Hf 5*d*	0.0024	0.0733
Si 3*p*	0.00017 (0.071)	0.0070 (0.095)
Si 3*s*	0.0010 (0.42)	0.0808 (1.10)
As 4*p*	0.0018 (0.75)	0.06045 (0.825)
As 4*s*	0.0017 (0.71)	0.1357 (1.85)

[a]The cross-sections from Ref. [40] are in units of mega-barns (Mb) whereas the cross-sections from Ref. [47] are proportional to the C 1s cross-section of 13,600 barns.

[b]The ratios of the cross-sections relative to the Hf 5*d* value are provided in parentheses. Between the two sets of values, the magnitudes of the *ns* cross-sections relative to the Hf 5*d* cross-sections differ significantly.

The fitted peak areas can then be related to the total electron population in $Hf(Si_{0.5}As_{0.5})As$, yielding cation and anion charges. To do this, the intensities must first be corrected for variations in cross-section (σ) and inelastic mean free path (IMFP, λ) [46]:

$$C_i = \frac{I_i/(\sigma_i\lambda_i)}{\sum_{j=1}^{n} I_j/(\sigma_j\lambda_j)}. \quad (1)$$

Because all observed photoelectron kinetic energies are similar throughout the valence band region, Eq. (1) can be simplified to Eq. (2) on the assumption that the IMFP values will be the same for all states:

$$C_i = \frac{I_i/(\sigma_i)}{\sum_{j=1}^{n} I_j/(\sigma_j)}. \quad (2)$$

Here, I_i/σ_i represents the intensity of the peak for a given atomic component under consideration and $\sum_{j=1}^{n} I_j/\sigma_j$ represents the sum of all the corrected peak intensities in the complete valence band spectrum. Peak 4 was adjusted assuming a 1:1 ratio of Si 3*p*:As1 4*p* states, whereas peak 5 was adjusted assuming a 2:1 ratio of As2 4*s*:Si 3*s* states. Following Eq. (2), the corrected and normalized component areas (C_i) were multiplied by the total valence electron population, which is 13.5 in the case of $Hf(Si_{0.5}As_{0.5})As$, to yield atomic charges. Two different sets of cross-sections were used (Table 4). The calculated electron populations per peak and the resulting average atomic charges determined from the spectrum shown in Fig. 9 and from a second sample (not shown) are given in Table 5. These charges suggest the formulation $Hf^{2+}[(Si_{0.5}As_{0.5})As]^{2-}$, consistent with the values deduced earlier through analysis of the As 3*d* and Si 2*p* binding energies. Moreover, it appears that both As1 and As2 have the same charge of 1−, in agreement with the observation of a single set of spin–orbit split As 3*d* peaks (Fig. 3a).

4. Conclusions

The metallic and Pauli-paramagnetic compound $Hf(Si_{0.5}As_{0.5})As$ is a new representative of the MAB series adopting the ZrSiS-type structure, exhibiting substitutional

Table 5
Electron population of valence states in $Hf(Si_{0.5}As_{0.5})As$ calculated using Eq. (2) and a total valence electron population of $13.5e^{-}$

State	Sample 1		Sample 2	
Cross-section (σ) reference	[40]	[47]	[40]	[47]
Hf 5*d* (peaks 1, 2)	1.5	1.8	1.9	2.3
As2 4*p* (peak 3)	5.1	5.2	4.8	4.9
As1 4*p*/Si 3*p* (peak 4)	5.8	6.0	5.8	5.8
As2 4*s*/Si 3*s* (peak 5)	0.9	0.4	0.8	0.4
As1 4*s* (peak 6)	0.2	0.1	0.2	0.1
Total Hf charge	2.5+	2.2+	2.1+	1.7+
Total anion charge $[(Si_{0.5}As_{0.5})As]$	2.5−	2.2−	2.1−	1.7−
Average charges[a]	2.1+ [Hf], 2.1− $[(Si_{0.5}As_{1.5})As]$			

[a]Scaling of the *ns* cross-sections from Table 4 such that both sets are similar did not alter the calculated charges to any appreciable degree (<0.1).

disorder of Si and As atoms within the denser square net of A atoms so that a narrow homogeneity range is possible in $Hf(Si_xAs_{1-x})As$ ($0.5 \leqslant x \leqslant 0.7$). It augments the few examples of anionic DFSO-stabilized materials now known. XPS core-line binding energy shifts in the Si 2*p* and As 3*d* spectra suggest the presence of anionic Si^{1-} and As^{1-}. The Hf 4*f* spectrum showed an asymmetric lineshape to higher BE, indicative of electronic delocalization, which enhances screening of the nuclear charge and attenuates the BE shift making it difficult to determine the Hf charge. By comparison to band structure calculations, the valence band spectrum was decomposed into Hf 5*d* states at the Fermi edge, followed by As1, As2, and Si *np* and *ns* states. Valence band spectra collected at different excitation energies as well as resonant PES measurements revealed that Hf $5d_{5/2}$ and $5d_{3/2}$ spin–orbit doublet peaks were present in the uppermost region, nearest to the Fermi edge. With the different component states now identified and fitted in the valence band spectrum, their electron populations were calculated to yield the formulation $Hf^{2+}[(Si_{0.5}As_{0.5})As]^{2-}$. This charge assignment differs substantially from that predicted by a simple electron-counting scheme, $Hf^{4+}(Si_{0.5}As_{0.5})^{1-}As^{3-}$, in which full electron transfer from Hf is assumed. Because X-ray spectroscopy provides an experimental probe and a more realistic evaluation of atomic charges, these results lead to the conclusions that: (i) MAB compounds with the ZrSiS-type structure, in general, possess substantial covalent bonding character, (ii) their metallic behaviour largely originates from hybridization of states from the atoms in the less dense square nets of M and B atoms, and (iii) the charges of the A and B atoms are similar despite their chemical inequivalence.

Acknowledgments

The Natural Sciences and Engineering Research Council of Canada (NSERC) supported this work through Discovery Grants to RGC and AM. NSERC, Alberta Ingenuity, and the University of Alberta provided financial support to APG. Dr. R. McDonald and Dr. M. J. Ferguson (X-ray Crystallography Laboratory) collected the single-crystal X-ray diffraction data, and Ms. C. Barker (Department of Chemical and Materials Engineering) assisted with the SEM-EDX analysis. Access to the Kratos XPS was provided by the Alberta Centre for Surface Engineering and Science, established with capital funding from the Canada Foundation for Innovation, which also bestows interim operating support, and from Alberta Innovation and Science. Dr. J. Thompson is thanked for help in carrying out the PES measurements at 11-ID.1 at the Canadian Light Source, which is supported by NSERC, NRC, CIHR, and the University of Saskatchewan.

References

[1] C. Wang, T. Hughbanks, Inorg. Chem. 34 (1995) 5524–5529.
[2] W. Tremel, R. Hoffmann, J. Am. Chem. Soc. 109 (1987) 124–140.
[3] F. Hulliger, J. Less-Common Met. 16 (1968) 113–117.
[4] R. Lam, A. Mar, J. Solid State Chem. 134 (1997) 388–394.
[5] M. Schmidt, T. Cichorek, R. Niewa, A. Schlechte, Y. Prots, F. Steglich, R. Kniep, J. Phys.: Condens. Matter 17 (2005) 5481–5488.
[6] R. Wawryk, A. Wojakowski, A. Pietraszko, Z. Henkie, Solid State Commun. 133 (2005) 295–300.
[7] S.-M. Park, S.-J. Park, S.-J. Kim, J. Solid State Chem. 140 (1998) 300–306.
[8] A. Kimura, S. Suga, T. Matsushita, T. Kaneko, T. Kanomata, Solid State Commun. 85 (1993) 901–905.
[9] V.H. Tran, Z. Bukowski, J. Stępień-Damm, R. Troć, J. Solid State Chem. 179 (2006) 1401–1406.
[10] Y.C. Wang, K.M. Poduska, R. Hoffmann, F.J. DiSalvo, J. Alloys Compd. 314 (2001) 132–139.
[11] M. Yuzuri, J. Phys. Soc. Jpn. 15 (1960) 2007–2012.
[12] L.C. Gupta, S.K. Malik, R. Vijayaraghavan, Phys. Lett. A 28 (1968) 255–256.
[13] T.Z. Vitkina, N.D. Zhigadlo, V.M. Ryzhkovskii, Cryst. Res. Technol. 23 (1988) 945–948.
[14] A. Kimura, S. Suga, H. Matsubara, T. Matsushita, Y. Saitoh, H. Daimon, T. Kaneko, T. Kanomata, Solid State Commun. 81 (1992) 707–710.
[15] A. Kimura, S. Suga, T. Matsushita, H. Daimon, T. Kaneko, T. Kanomata, J. Phys. Soc. Jpn. 62 (1993) 1624–1633.
[16] A.P. Grosvenor, S.D. Wik, R.G. Cavell, A. Mar, Inorg. Chem. 44 (2005) 8988–8998.
[17] A.P. Grosvenor, R.G. Cavell, A. Mar, Phys. Rev. B 74 (2006) 125102/1–125102/10.
[18] A.P. Grosvenor, R.G. Cavell, A. Mar, Chem. Mater. 18 (2006) 1650–1657.
[19] G.M. Sheldrick, SHELXTL, version 6.12, Bruker AXS Inc., Madison, WI, 2001.
[20] L.M. Gelato, E. Parthe, J. Appl. Crystallogr. 20 (1987) 139–143.
[21] C. Morant, L. Galan, J.M. Sanz, Surf. Interface Anal. 16 (1990) 304–308.
[22] N. Fairley, CasaXPS, version 2.3.9, Casa Software Ltd., Teighnmouth, Devon, UK, 2003.
[23] D. Briggs, Surface Analysis of Polymers by XPS and Static SIMS, Cambridge University Press, Cambridge, 2005.
[24] T. Regier, J. Paulsen, F. Wright, I. Coulthard, K. Tan, T.K. Sham, R.I.R. Blyth, AIP Conf. Proc. 879 (2007) 473–476.
[25] O.K. Andersen, Phys. Rev. B 12 (1975) 3060–3083.
[26] E. Dashjav, H. Kleinke, Z. Anorg. Allg. Chem. 628 (2002) 2176.

[27] T.J.B. Holland, S.A.T. Redfern, Mineral. Mag. 61 (1997) 65–77.
[28] L. Pauling, The Nature of the Chemical Bond, 3rd ed, Cornell University Press, Ithaca, 1960.
[29] P. Villars (Ed.), Pauling File Binaries Edition, version 1.0, ASM International, Materials Park, OH, 2002.
[30] H.F. Franzen, M. Köckerling, Prog. Solid State Chem. 23 (1995) 265–289.
[31] H. Kleinke, Trends Inorg. Chem. 7 (2001) 135–149.
[32] N. Soheilnia, A. Assoud, H. Kleinke, Inorg. Chem. 42 (2003) 7319–7325.
[33] B.J. Flinn, N.S. McIntyre, Surf. Interface Anal. 15 (1990) 19–26.
[34] C.D. Wagner, A.V. Naumkin, A. Kraut-Vass, J.W. Allison, C.J. Powell, J.R. Rumble Jr., NIST X-ray Photoelectron Spectroscopy Database, version 3.4 (web version), National Institute of Standards and Technology, Gaithersburg, MD, 2003 (srdata.nist.gov/xps).
[35] G. Petö, E. Zsoldos, L. Guczi, Z. Schay, Solid State Commun. 57 (1986) 817–819.
[36] O. Renault, R. Marlier, N.T. Barrett, E. Martinez, T. Baron, M. Gely, B. De Salvo, Surf. Interface Anal. 38 (2006) 486–488.
[37] C.M. Hessel, E.J. Henderson, J.G.C. Veinot, J. Phys. Chem. C 111 (2007) 6956–6961.
[38] S. Doniach, M. Šunjić, J. Phys. C: Solid State Phys. 3 (1970) 285–291.
[39] S. Hüfner, in: L. Ley, M. Cardona (Eds.), Photoemission in Solids II, Springer, Berlin, 1979.
[40] J.J. Yeh, I. Lindau, At. Data Nucl. Data Tables 32 (1985) 1–155.
[41] C.W. Thiel, H. Cruguel, H. Wu, Y. Sun, G.J. Lapeyre, R.L. Cone, R.W. Equall, R.M. Macfarlane, Phys. Rev. B 64 (2001) 085107/1–085107/13.
[42] J. Thompson, V. Arima, Y. Zou, R. Fink, E. Umbach, R. Cingolani, R.I.R. Blyth, Phys. Rev. B 70 (2004) 153104/1–153104/3.
[43] A.G. Thomas, W.R. Flavell, A.K. Mallick, A.R. Kumarasinghe, D. Tsoutsou, N. Khan, C. Chatwin, S. Rayner, G.C. Smith, R.L. Stockbauer, S. Warren, T.K. Johal, S. Patel, D. Holland, A. Taleb, F. Wiame, Phys. Rev. B 75 (2007) 035105/1–035105/12.
[44] J. Thompson, V. Arima, F. Matino, S. Berkebile, G. Koller, F.P. Netzer, M.G. Ramsey, R. Cingolani, R.I.R. Blyth, Synth. Met. 153 (2005) 233–236.
[45] D. Briggs, J.C. Rivière, in: D. Briggs, M.P. Seah (Eds.), Practical Surface Analysis, Vol. 1, Auger and X-ray Photoelectron Spectroscopy. 2nd ed., Wiley, Toronto, 1990.
[46] J.F. Watts, J. Wolstenholme, An Introduction to Surface Analysis by XPS and AES, Wiley, Rexdale, 2003.
[47] J.H. Scofield, J. Electron Spectrosc. Relat. Phenom. 8 (1976) 129–137.